Effervescence-Inspired Self-Healing Plastrons for Long-Term Immersion Stability

William S. Y. Wong* and Doris Vollmer*

The use of superhydrophobic/superamphiphobic surfaces demands the presence of a stable plastron, i.e., a film of air between micro- and nanostructures. Without actively replenishing the plastron with gases, it eventually disappears during immersion. The air diffuses into the immersion liquid, i.e., water. Current methods for sustaining the plastron under immersion remain limited to techniques such as electrocatalysis, electrolysis, boiling, and air-refilling. These methods are difficult to implement at scale, are either energy-consuming, or require continuous monitoring of the plastron (and subsequent intervention). Here, the concept of passive on-demand recovery of the plastron via the use of a chemical reaction (effervescence) is presented. A superhydrophobic nanostructured surface is layered onto a wetting-reactive, gas-forming (effervescent) sublayer. During extended exposure to moisture, the effervescent layer must be protected by a moisture-absorbent, water-soluble polymer. Under prolonged immersion, partial collapse of the Cassie-state induces contact of water with the effervescent layer. This induces the local formation of gases from effervescence, which restores the Cassie-state. These facile and scalable design principles offer a new route toward intervention-free and immersion-durable superhydrophobic/superamphiphobic surfaces.

1. Introduction

The ability to trap gases underwater by superhydrophobic/superamphiphobic surfaces has demonstrated potential for many applications: antifouling,[1] anti-biofouling,[2] waterproofing wearable electronics,[3,4] antibubbling/foaming,[5–8] drag reduction,[9] and even electrocatalysis.[10,11] During immersion, a trapped layer of gases, the so-termed plastron, forms a film interfaced with the surrounding liquid, i.e., water. In Nature, well-oxygenated water is known to sustain durable breathable oxygen plastrons for underwater insects such as the *Canace nasica*.[12] The aquatic plant, *Salvinia molesta*, prolongs the lifetime of its plastron by pinning the water–air interface (energetic minima) at the hydrophilic tips on its hydrophobic structures.[13] Despite the potential exposure to immersion, most

W. S. Y. Wong, D. Vollmer
Max Planck Institute for Polymer Research
Ackermannweg 10, D-55128 Mainz, Germany
E-mail: wong@mpip-mainz.mpg.de; vollmerd@mpip-mainz.mpg.de

The ORCID identification number(s) for the author(s) of this article can be found under https://doi.org/10.1002/adfm.202107831.

man-made superhydrophobic surfaces are not designed[14] for immersion. They have comparatively large micropores,[15] bearing low impalement or water-entry pressure. Therefore, the so-termed Cassie[16]-to-Wenzel[17] transition easily occurs, accompanied by the disappearance of the plastron. Artificial plastrons typically deplete due to gas diffusion,[18,19] or hydrodynamic shear[20] amongst other mechanisms.[21] To counter these challenges, active methods have been devised to retain or recover plastrons: including the catalysis of chemical agents (oxidizers) in the liquid medium,[22] electrocatalysis for gas-generation,[23–26] heat-induced boiling,[27] or even the direct replacement of air through porous substrate media.[28–30] These methods are, however, difficult to implement at scale and requires intermittent or continuous energy input. Passive approaches aim to increase plastron robustness and pressure equalization,[31] with the use of hierarchical roughness or re-entrancy.[32,33] In contrast to active methods, these techniques are not able to repair damages to the plastron.

In this work, we introduce a passive on-demand approach. We term this concept "on-demand" because gases are only produced if the plastron is damaged. The strategy is simple: It combines the use of 1) dense nanostructural packing[34,35] to ensure high impalement pressure and rapid gas absorption, supported by 2) wetting-activated gas forming sublayer (effervescent materials) for plastron repair. The plastron autonomously heals during Wenzel[17]-wetting, i.e., only when wetted. To the best of our knowledge, the use of reaction-induced methods toward plastron repair and regeneration has never been explored.[1,9] Here, we leverage on the effervescence-effect, i.e., the formation of gases in a liquid by chemical reaction.
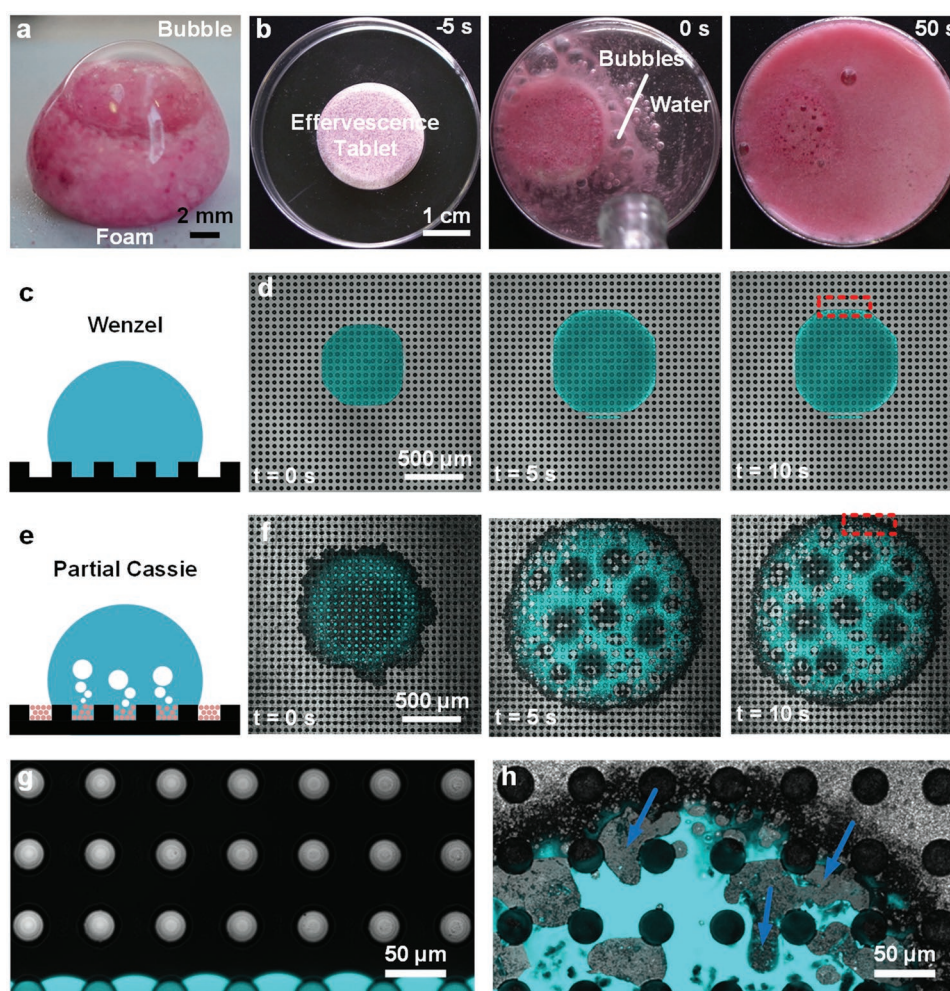
To showcase our proof-of-concept, we used an acid-base reaction: sodium bicarbonate ($NaHCO_3$) and citric acid ($C_6H_8O_7$) to produce carbon dioxide (CO_2). CO_2 was chosen on the basis of its plastron longevity in low pH (5–6) freshwater (carbonate equilibria), benign by-products (sodium citrate), and excellent processability for coatings (dispersibility and dormancy as solids). The reactivity of the CO_2 gas-forming layer (GL) for plastron-regeneration was assessed and confirmed via confocal and optical microscopy with model micropillar structured surfaces. To bring the concept to scale, a four layer coating (Quad) was fabricated, ensuring optimal mechanical stability and longevity: 1) a base layer (ethyl cellulose, EC), 2) the gas-forming layer ($NaHCO_3$–$C_6H_8O_7$, GL), 3) a condensation-protection layer (polyvinylpyrrolidone, PVP), and a 4) functional

**ADVANCED
SCIENCE NEWS**
www.advancedsciencenews.com

**ADVANCED
FUNCTIONAL
MATERIALS**
www.afm-journal.de

Figure 1. Concept: effervescence-inspired regeneration of plastrons. Effervescent material forming a) a foamy, bubbly aqueous drop after contacting a water drop on a superhydrophobic surface. b) Vitamin C tablet (left) forming CO_2 foams and when in water (center and right). Model SU8 micropillar surfaces (pillar diameter: d = 30 µm; center-to-center distance: l = 60 µm; height: h = 20 µm), c,d) without and e,f) with the effervescent gas-forming layer (GL), schematized as pink microparticles. A stoichiometric ratio of $NaHCO_3$–$C_6H_8O_7$ was used. Water is represented as blue, dyed via a fluorescent dye: ATTO 488. (c,d) Wenzel-wetting was evident in the control. (e,f) A partial Cassie state (bubbles and dry zones visible as dark grey areas) was achieved with the presence of the gas-forming layer despite the comparative hydrophilicity of the surface. High magnification of the contact line at drop edges shows (g) a stable equilibrium contact line that wets the surface and (h) an unstable contact line that is continuously being pushed back by the effervescence-induced formation of gas bubbles. The gas-forming layer appears as grainy patches between black micropillars, top view.

superhydrophobic layer (fluoro-functionalized silica, superhydrophobicity (SH)).[36] We demonstrate long-term immersion stability (unaffected wetting performance with low- and high-surface tension liquids) for more than two months. The coating also withstands high-speed liquid drop impact (up to 6 m s^{-1}), analogous to rain drops.

2. Results and Discussion

2.1. Effervescence for Resisting the Wenzel State

The effervescence-effect is found in many benign chemical reactions (**Figure 1**a,b). With the objective of developing a stable plastron, gases produced from effervescence should preferentially

experience slow natural dissolution into the surrounding water phase. Three common effervescent gases (Figure S1, Supporting Information) were thus tested (hydrogen, H_2, nitrogen, N_2, and carbon dioxide, CO_2). Amongst these gases, CO_2 gas bubbles and plastrons were comparatively more stable in the surrounding water phase within the first 24 h (Figure S1, Supporting Information), but also more than 8 weeks in continued tests (Figure S2, Supporting Information).

To assess the behavior of wetting-reactive effervescence, model micropillar structured surfaces were first investigated. A stoichiometric ratio of sodium hydrogen carbonate and citric acid ($NaHCO_3$–$C_6H_8O_7$, 20 mg mL^{-1}, dispersed in acetone) was spray-coated (2 bars, working distance of 10 cm) onto model micropillar arrays. After evaporation of the acetone, the array was filled with $NaHCO_3$–$C_6H_8O_7$ particulate solids. During

contact with water, the solids experience hydrolysis and a prompt acid–base reaction, producing gaseous CO_2.

$$3NaHCO_3 + C_6H_8O_7 \rightarrow Na_3C_6H_5O_7 + 3CO_2 + 3H_2O \quad (1)$$
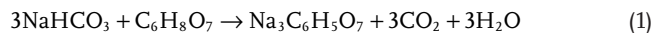
The actual loading is ≈7.5 mg of solids per cm^2. Considering the stoichiometric ratio used, this would contain 4.3 mg or 0.05 mmol of sodium hydrogen carbonate, which yields 0.05 mmol of carbon dioxide. At room temperature and pressure (RTP, 298 K/25 °C) conditions, this gives a theoretical maximum yield of 1.2 cm^3 of gases per cm^2. However, the actual yield is less. Using weight measurements, the actual yield of spray-coated layer of GL is ≈34% of the theoretical yield, which leads to ≈0.4 cm^3 of gases per cm^2. Therefore, considering a plastron that is 10 μm thick, this gas reservoir can refill the plastron by up to 400 times (400 times 10 μm) before disintegration. However, this assumes that no further operational degradation occurs during its usage.

This CO_2 gas-forming layer is hereinafter referred to as the GL for brevity. Mild polishing[37] was performed to remove $NaHCO_3$–$C_6H_8O_7$ from the tops of pillars to aid in confocal microscopic observations. These GL-micropillars and a control micropillar array (without GL) were then wetted by a drop of water (fluorescently dyed, 2 μL).

With control micropillars, we noted the complete wetting (Wenzel-state[17]) of the micropillar array (dark gray circles, Figure 1c,d; Movie S1, Supporting Information). Top-view confocal images (Figure 1d; Movie S1, Supporting Information) reveal that the water contact line (cyan) progresses smoothly (Figure 1g for higher magnification; Movie S1, Supporting Information). In the GL-coated micropillars, we noted multiple light or dark gray locations within the drop that remained dry, i.e., bubble-on-surface (Figure 1e,f; Movie S1, Supporting Information). These regions do not contain fluorescent dye, i.e., they are covered in gas bubbles. The formation and trapping of bubbles create a partial Cassie[16] state (Figure 1f). At the drop edge, the contact line is highly distorted (Figure 1h for higher magnification; Movie S1, Supporting Information). The moving water contact line appeared to be continuously pushed back by the effervescence-effect. These experiments demonstrate the feasibility of effervescence in the local reversal of Wenzel-wetting, although a stable Cassie-state was not realized. This was expected since the micropillar array was not superhydrophobic.

2.2. Effervescence for Plastron Repair/Recovery during Pressurized Immersion

To stabilize the gases formed by effervescence, the control and GL-infiltrated micropillar arrays were sequentially coated (light gray spheres, **Figure 2**a,b) using hydrophobic nanoparticles (see Methods and Discussion in the Supporting Information). SEM images reveal that the control and GL-coated micropillars were covered with an ≈1–3 μm thick layer of agglomerated nanoparticles (patchy in coverage, Figure S3, Supporting Information). To demonstrate on-demand gas formation, hydrocarbon-functionalized nanoparticles were used, which allowed improved penetration of water into the coating.

To quantify the degradation and recovery of the Cassie-state, we used a custom-built pressure chamber (V = 10 mL, Figure S4, Supporting Information). A syringe pump pressurizes the system. The pressure was increased up to 2 bars within 50 s. Over the next 10 min, the pressure equilibrates to ≈1.8 bars, Figure 2e,f, black line. During this time, we simultaneously monitored and quantitatively assessed the reflectivity of the plastron (Figure 2e), using a bright-field optical microscope. This protocol allows for real-time observations of impalement/recovery events within the timescale of several minutes. This reflects the more natural state of plastron degradation, i.e., not by en masse impalement[35] but by microscopically failing domains.[38] Reflectivity was tracked using an algorithm that captures the intensity of the reflection. Reflection intensities were normalized across each experiment (0–100%).

Bright images suggest the presence of the plastron while darkened images is indicative of surface wetting. Without the GL-coating, plastron reflectivity first decreased to ≈70% due to initial plastron compression. After 300 s, plastron reflectivity drops sharply (Figure 2c,e; Movie S2, Supporting Information), caused by localized wetting, resulting in a mosaic pattern of black (impaled, Wenzel) and white (not impaled, Cassie) domains (Figure 2e, inset). During this period, the black patches propagate across the surface, causing an irreversible decrease in plastron reflectivity. A Cassie-to-Wenzel transition occurs. With the GL-coating, the mosaic patterns are no longer easily observable as the multilayers obscured the micropillar arrays (Figure S3, SEMs, Supporting Information). The initial image (Figure 2d, 0 s) shows the presence of a plastron. The overall reflectivity decreased immediately after the pressure was applied, accompanied by the complete loss of plastron reflectivity by 300 s. The images darken (Figure 2d, 300 s). After 400 s, the plastron reflectivity spontaneously brightens, hinting of plastron regeneration (Figure 2d,f; Movie S2, Supporting Information). Impalement of water into the coating induced the effervescence-reaction, see Movie S2 and Figure 2f inset for a zoomed-in image of the regenerated surface. The normalized reflectivity even exceeded its initial state (70%), as shown by the maxima (100%) at 500 s. The effervescence-reaction produced a thicker plastron layer than the original superhydrophobic surface. However, this microscopically-recovered plastron does not persist. This is likely due to the high applied pressure: any CO_2 formed dissolves into the surrounding water and the plastron depletes. Notably, the time-scale of impalement depends on the applied pressure and coating variations.[38,39]

2.3. Scale-Up Design (from Model Surface to Quad-Layered Coatings)

Next, we aim to port the concepts and understanding from the impalement and recovery of model micropillar arrays to scalable coatings (see the Experimental Section for details). First, a base layer of EC polymer (0.05 g mL^{-1} in toluene:acetone at 4:1 v/v) was deposited via spin-coating (500 RPM, 60 s) on a glass substrate (**Figure 3**a,e-1). The smooth base EC layer is hydrophilic but invariant toward wetting (Figure 3a, top and side view images of a deposited drop and Figure S5, black line,
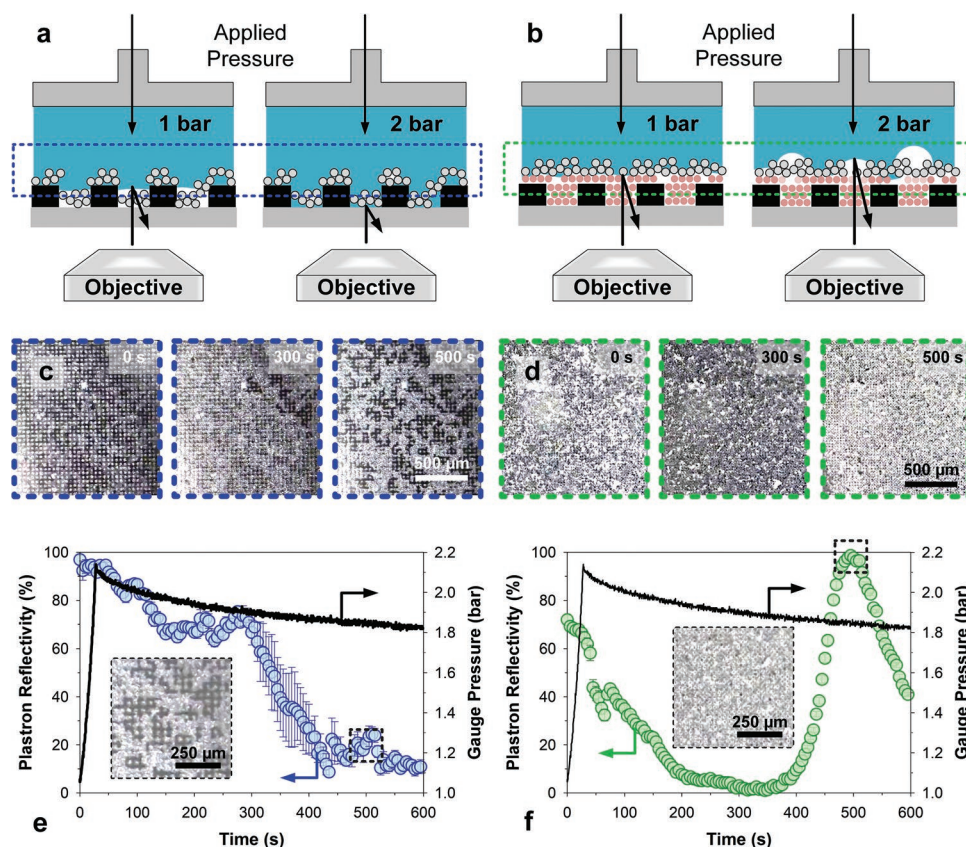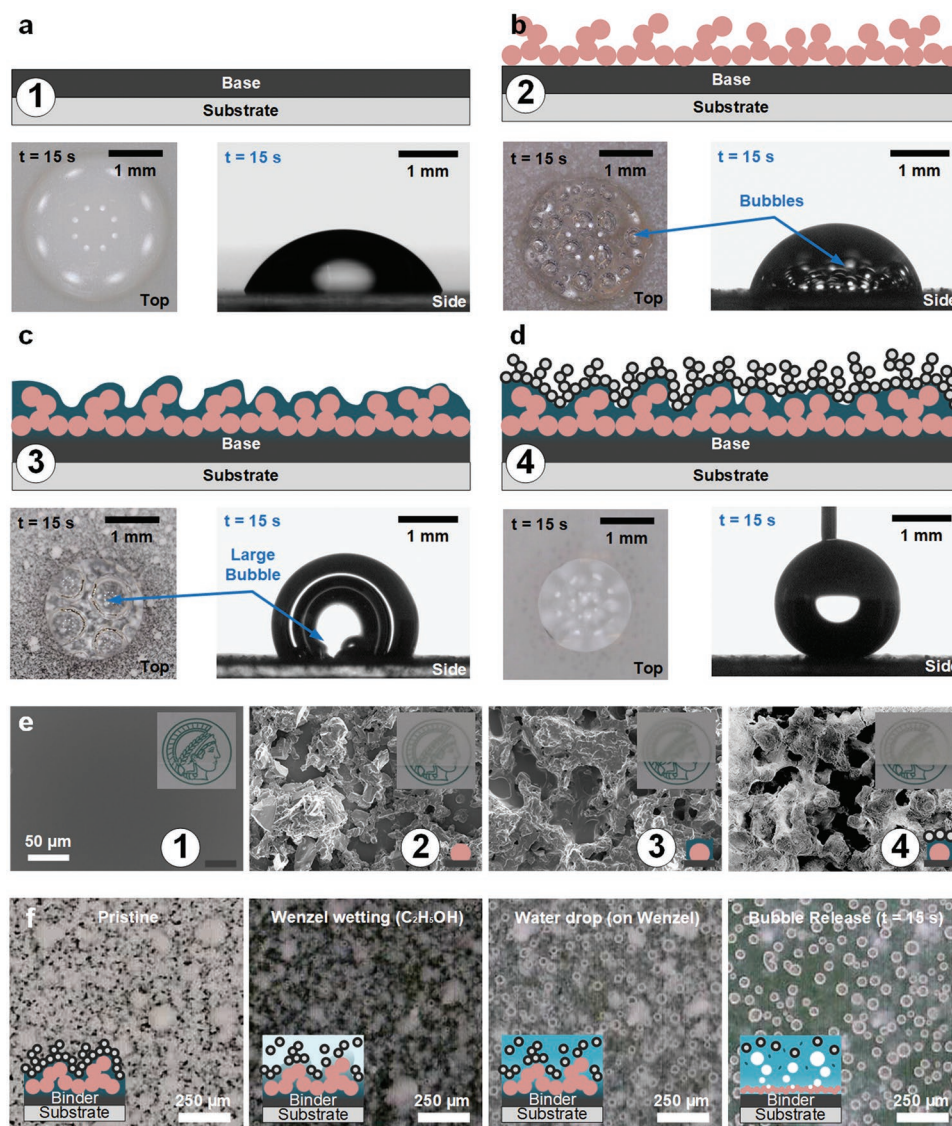
Figure 2. Plastron regeneration: pressurized immersion of an effervescence gas-forming layer (GL) with a nanoparticle-based superhydrophobic surface. Surface plastron monitoring of a,c) hydrophobic nanoparticles-on-micropillars and b,d) hydrophobic nanoparticles-on-GL-on-micropillars under 1 bar of applied liquid pressure (corresponds to 10 m H_2O column) in the imaging chamber. The variation in surface reflectivity represents the presence (bright) or absence (dark) of a plastron. Bright and dark regions represent the local Cassie- and Wenzel-states respectively. (a,c) Without the GL (gas-forming microparticles colored red), the penetration of liquid into the nanoparticle surface (light gray spheres) results in (c) dark zones. b,d) With GL, the penetration of liquid starts, but is halted and prevented by the GL upon wetting-contact reaction. (d) The entire surface brightens with the local formation of air bubbles and the regenerated plastron. Contrast–brightness adjustments were made using a thresholding script in ImageJ. e,f) The overall reflectivity of the plastron can be quantitatively evaluated by mapping the color intensity at several different locations (insets: magnified images of surfaces). GL: gas-forming layer.

Supporting Information). This base layer later serves to encapsulate the wetting-reactive GL.

Second, the wetting-reactive effervescent GL was deposited via spray-coating (Figure 3b). As per before, a stoichiometric ratio of the GL was dispersed in acetone at 20 mg mL^{-1} and spray-coated onto the EC layer. Scanning electron images show that surface morphology is microstructured (Figure 3e-2). The transparency of the surface decreases. The EC–GL layers are hydrophilic and wetting-reactive, rapidly forming bubbles during drop wetting (Figure 3b, top and side view images of a deposited drop), This results in small increments to static contact angles during deposition (Figure S4, blue line, Supporting Information). The GL is highly reactive to moisture. Notably, even condensation of water vapor from a near-field water source (immersion) into the superhydrophobic layer can trigger a premature effervescence reaction. The stability of bulk GL material at different humidities is analyzed using a climate chamber[37,40] (exposure time: 30 min). The exposure time of 30 min exceeds the preparation time for the PVP–GL layer (typically 10–20 min). To analyze moisture sensitivity, a mass and reactivity loss analysis was performed (see Discussion and

Table S1, Supporting Information). We noted a loss of 17% in net reactivity only at the maximum tested humidity (95%).

To prevent condensation-induced effervescence and the accompanied breakup of the coating (Figure S6 and Movie S3, Supporting Information), we shielded the GL with a thin layer of PVP (Figure 3c). Within the plastron, a relative humidity of 100% exists (the state of immersion). PVP under a 100% relative humidity will experience swelling, saturating at ≈0.5 volume fraction water. The literature[41] suggests that a thickness independent diffusion coefficient of 10^{-11} cm^2 min^{-1} drives the moisture flux. The absorption kinetics are relatively unaffected by the nature of the substrate layer (underlying layers).[41] Notably, the PVP remains fully intact even under an almost condensing environment (100% relative humidity). Only direct water contact can lead to dissolution. The PVP prevents the GL from direct exposure to the humid plastron. Long-term exposure (21 weeks) of the GL–PVP component is studied in both in-air and under-water exposure. Both variants retained effervescent (bubble-release) properties, withstanding all ambient modes of storage/operation conditions (Figure S5, Supporting Information).

**ADVANCED
SCIENCE NEWS**
www.advancedsciencenews.com

**ADVANCED
FUNCTIONAL
MATERIALS**
www.afm-journal.de

Figure 3. Scale-up: multilayer coating concept. a–e) Four distinct layers were developed. (a) A base layer of ethyl cellulose, EC is coated with (b) a gas-forming layer, GL (NaHCO$_3$–C$_6$H$_8$O$_7$) before being sealed with (c) a condensation-protection layer, polyvinylpyrrolidone, PVP. The final supehydrophobic (SH) functional layer of fluoro-functionalized silica is then deposited on these microstructured agglomerates. The SH layer is superaerophilic, thus absorbing and stabilizing any produced gases. (e) Optical and scanning electron microscopy imaging of the four layers showing the microstructuring and optical opacity. The release of (f) gas from Wenzel-wetting is showcased in a drop-based (ethanol-assisted) activation. In this case, the surface is destroyed in entirety to release gases. EC: ethyl cellulose polymer; GL: gas-forming layer; PVP: polyvinylpyrrolidone; SH: superhydrophobic/superamphiphobic. Quad layer: EC–GL–PVP–SH.

The water-absorbent and water-soluble PVP layer is formed rapidly to prevent the dissolution of the base EC layer. Spin-coating of PVP dissolved in ethanol (20 mg mL^{-1} at 2000 RPM) onto the EC–GL layers completes the condensation-protection layer. SEM images revealed that the morphology remained unaltered (Figure 3e-3). The EC–GL–PVP is slightly hydrophobic (Figure 3c, top and side view images of a deposited drop). The delayed formation of bubbles during drop wetting (water-dissolving PVP) still results in small increments to the advancing contact angle (Figure S6, red line, Supporting Information). Notably, the combination of the sublayer roughness and gas-evolution appears to be sufficient in enabling contact

line pinning thus keeping the contact angle high (inhibiting drop spreading, Figure S7 and Movie S4, Supporting Information). As these contact angles are determined by pinning of contact lines, the value depends on the local coating morphology and how the drop is deposited (e.g., if the drop is squeezed onto the surface).

To confer nanostructured SH, a functional layer of fluoro-functionalized nanosilica (10 mg mL^{-1} acetone) was spray-coated onto the EC–GL–PVP layers. Deposition of the nanostructures is conformal and does not visibly alter the base microstructures (Figure 3e, 2nd panel vs 4th panel; Figure S8, Supporting Information). The final EC–GL–PVP–SH layered

**ADVANCED
SCIENCE NEWS**
www.advancedsciencenews.com

**ADVANCED
FUNCTIONAL
MATERIALS**
www.afm-journal.de

surface (Figure 3d) is superhydrophobic (also superamphiphobic) as per Figure 3d, top/side view insets. It is invariant toward wetting, as per Figure S6 of the Supporting Information, purple line. This four-layer sandwich (EC–GL–PVP–SH) is hereinafter referred to as the Quad-layer.

To test the wetting-reactivity of the surface, we deliberately Wenzel-wetted it with very low surface tension liquids, i.e., ethanol (Figure 3f, first panel). Thereafter, addition of a drop of water will dissolve the PVP layer and successively trigger wetting-reaction and the effervescence-effect. This on-demand property leads to the release of bubbles (Figure 3f, last panel). After the surface is dried, bubbles are released and superhydrophobicity is retained (Figure S9, Supporting Information). The static contact angle is barely affected (160°) but the roll-off angle is increased, with a much larger standard deviation due to the surface inhomogenity and pinning (10° ± 6°).

2.4. Mechanism of Long-Term Infiltration and Recovery

The Cassie-to-Wenzel transition often begins at certain defect[38,42] sites (**Figure 4**a, panel 1). Water first wets through micro-pores in the superhydrophobic structure before penetrating the nanopores. Depending on the applied pressure and dissolved gas content of the water phase, this can take between days[19] to weeks.[35] With the Quad-layered design, water proceeding into the surface will eventually encounter the water-soluble PVP layer. After dissolving the PVP, water contacts the GL sub-layer (Figure 4a, 2nd and 3rd panels). Once the wetting-induced reaction occurs, the contact line will be repelled outward due to the gas-evolution reaction (Figure 4a, 4th panel). The reaction stops. Condensation-induced damages do not appear to affect this localized process as coatings remain intact.

To test the long-term behavior, pristine superamphiphobic Quad-layered and control fluorinated soot-templated[43] surfaces were immersed into 20 cm of water for 8 weeks (Figure 4b). To quantify possible damage of the surface after immersion, we measured the roll-off angles (Figure 4c,d) on pristine (nonimmersed) and 8 weeks-immersed surfaces across a variety of liquids (see the Experimental Section). In the pristine state, both soot-templated and Quad-layered surfaces were superamphiphobic (roll-off angle < 10°, 6 µL) with a surface tension limit of 27.4 mN m^{-1} (hexadecane). Immersed soot-templated surfaces suffered from a pronounced loss in roll-off angle performance. The roll-off angle increased by +10° to +20° with all test liquids (Figure 4c). On the contrary, immersion did not change the roll-off angle of Quad-layered surfaces. Within experimental accuracy, the roll-off angles were identical before and after immersion (Figure 4d).

Scanning electron and optical microscopy (Figure S10, Supporting Information) revealed that soot-templated surfaces suffered from a loss in coating integrity after long-term immersion. Large portions of the coating were removed (Figure 4e, 2nd and 3rd magnified panel). The immersed Quad-layered surfaces also revealed an altered morphology after immersion (Figure 4f). Select microlocalities showed the presence of microscopic holes (Figure 4f, 2nd and 3rd magnified panel). These zones are ≈200 µm in diameter, and are likely to be the domains that were penetrated, recovered, and

thus reconfigured (Figure 4a, 3rd and 4th panels). The size of these domains matches the size of liquid penetration (order of 100 µm) that were previously observed for superhydrophobic/superamphiphobic surfaces.[38,39,42] The real-time direct observations (within minutes) of nanoimpalement and effervescence remain difficult because liquid penetration is too slow.

2.5. Drop Impact Wetting: Low to High Velocities

Would the wetting-reactive layers (GL–PVP) fail during high-speed drop impact due to penetration, impalement, and reaction?[44,45] To answer this question, a series of low- to high-speed drop impact experiments were performed on soot-templated, EC–SH (w/o GL) and Quad-layered surfaces (**Figure 5**a). This tests two key parameters: 1) Influence of a porous nanostructure (soot-templated) and 2) influence of the presence/absence of the wetting-reactive layers, GL–PVP (EC–SA vs Quad-layered). Drops were allowed to impact surfaces from a height of up to 1 m. The drop velocity, v, ranged from 1 to 6 m s^{-1} with We numbers of ≈36 to 1300.

The terminal velocity, v, of a drop (i.e., raindrop)[46] is dependent on drop size, balanced between gravitational and drag force, $mg = \frac{1}{2}\rho v^2 C_D \pi r^2$. m and r are the drop mass and radius (1.2×10^{-3} m) respectively, ρ is the density of air (1.2 kg m^{-3}), g is the gravitational constant (9.81 m s^{-2}), C_D is the drag coefficient which depends on the Reynolds number. Terminal velocity, v, under these conditions reaches up to 6–7 m s^{-1}.[46] For impaled soot-templated surfaces (with + symbol), measured and reported timescales represent an underestimate as impaled drops may be stuck on the surface indefinitely (i.e., $t_{contact} = \infty$, Movie S5, Supporting Information). In this event, the timing is obtained after achieving its maximum rebounding extension (Figure 5c). Full drop impact frames at high speeds are included in Figure S11 of the Supporting Information.

At low impact velocity (1–2 m s^{-1}), all surfaces behave identically. Impacted drops experience Rayleigh-Plateau instabilities[47] that eject a satellite droplet (Figure 5b,c; Movie S6, Supporting Information). At higher impact velocity (i.e., 3–6 m s^{-1}), drops impacting soot-templated surfaces stayed primarily as a single impaled drop having a few satellite droplets, per Figure 5b,d,e and Movie S7 (Supporting Information). EC–SH and Quad-layered surfaces exhibit fragmentation behavior. Drop impact time continues to decrease, reaching instances of ≈1–4 ms in both cases. This drop fragmentation capability in Quad-layered surfaces is likely attributed to the nanoparticulate layer (per EC–SH) and how it prevents impalement while splitting the drop.[48] Even at the highest impact velocity (thus deepest penetration), the coating remained stable and intact, hinting toward good performance of the Quad-layered surfaces during heavy rain.

3. Conclusions

Immersion-stability is crucial toward the future design, fabrication, and application of superhydrophobic/superamphiphobic surfaces. Currently, the focus has been on properties such as in-air contact angles, low roll-off angles, and low contact angle
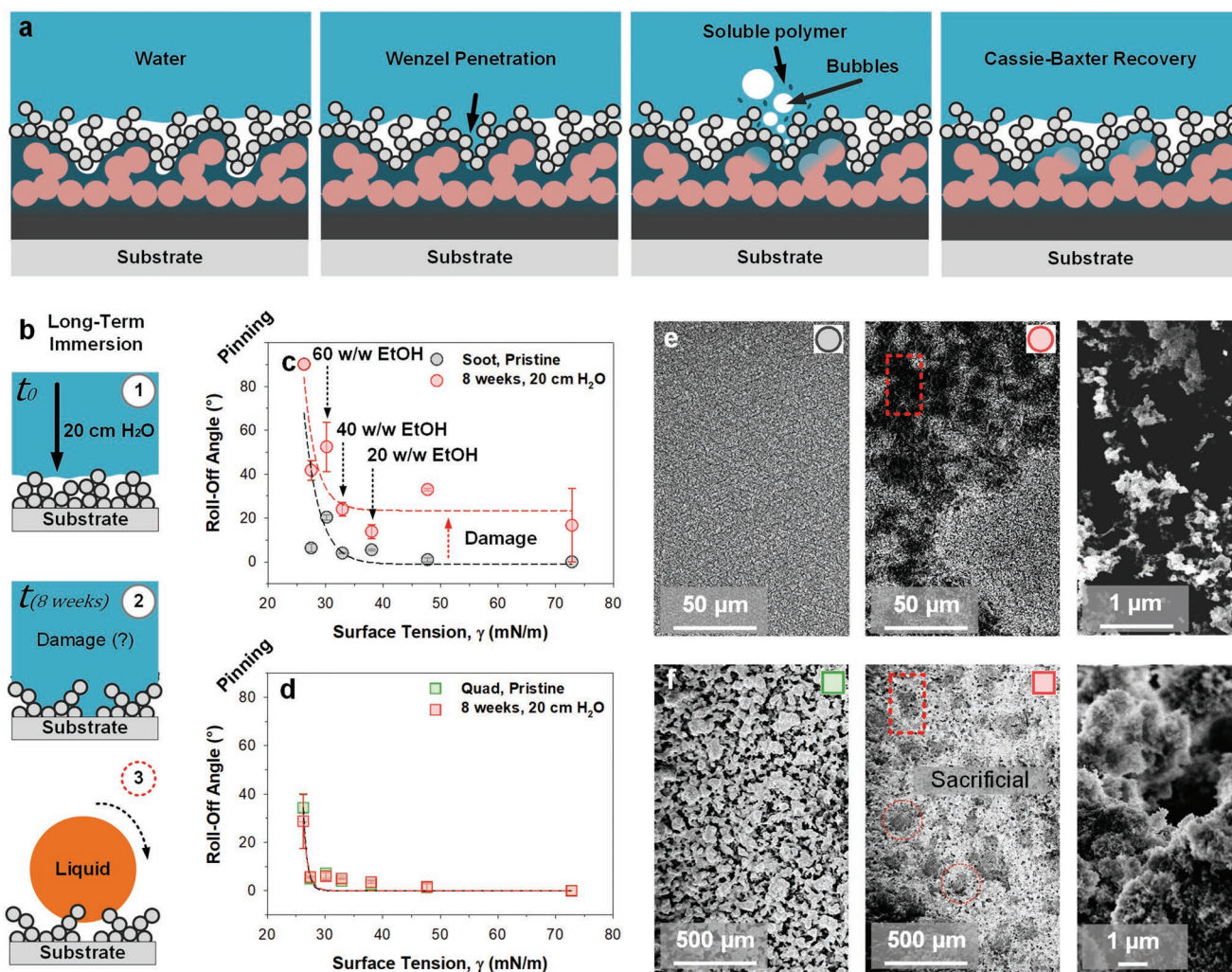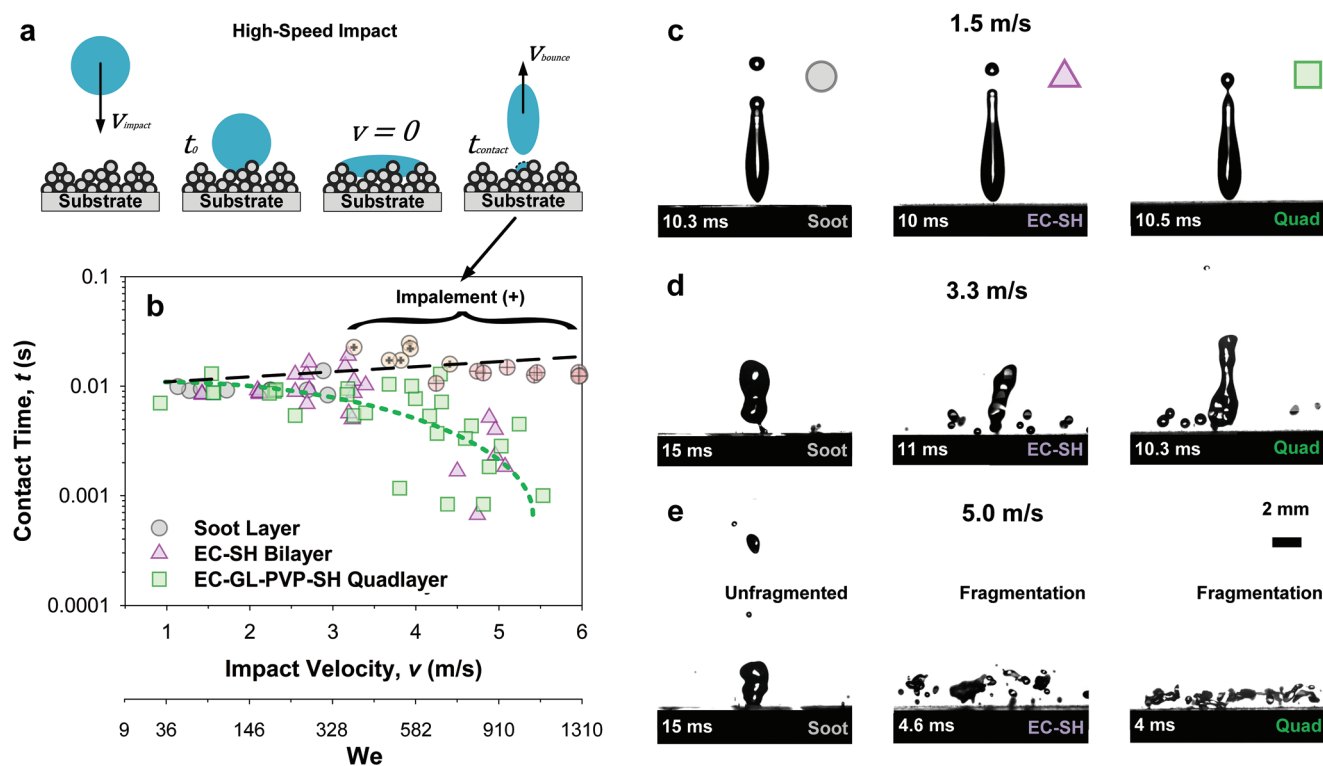
Figure 4. Long-term immersion and regeneration. a) Local Wenzel-penetration of the surface leading to a gas-forming reaction (upon breaking through the nanopores), giving rise to bubbles that rapidly repairs the functional plastron. b) Coated test surfaces (soot-templated and Quad-layered) superhydrophobic surfaces were immersed inside a tank with 20 cm height water. They were then left for 8 weeks. c,d) Pristine Quad-layered and soot-templated surfaces were evaluated alongside immersed surfaces in order to evaluate superdewetting durability (both water and low surface-tension liquids). e,f) Soot-templated nanoparticle surfaces suffered from failure in coating integrity, with nanoparticle patches stripped off the surfaces. (f) The Quad-layered surfaces appeared compressed with locally deformed spots (diameters of ≈200 μm). These spots are likely locations where Wenzel-wetting spontaneously occurred as "sacrificial spots," thus leading to GL activation. Notably, both local and surrounding micro- and nanostructures remained intact, albeit reorganized. EC: ethyl cellulose polymer; GL: gas-forming layer; PVP: polyvinylpyrrolidone; SH: superhydrophobic/superamphiphobic. Quad layer: EC–GL–PVP–SH.

hysteresis. These requirements entail high interstitial spacing and low solid fraction.[14,49] However, long-term immersion (i.e., underwater) stability requires complementary design parameters. This is where on-demand plastron repair is crucial. During failure of the Cassie-state, contact of water with an effervescent material layer results in gas formation via a wetting triggered chemical reaction. These gases are then absorbed into the nanostructures, enabling on-demand wetting-induced plastron repair. Together with small interstitial spacing which enables counter-wetting capillary pressure,[34,35,37] the slow and localized contact line progression (Wenzel transition) can be countered. This work provides the first instance where an immersion-stable, wetting-reactive sublayer is integrated into a superhydrophobic coating in order to execute on-demand plastron recovery.

4. Experimental Section

Synthesis of Model Surfaces (Control and Infiltrated Micropillar Arrays): Micropillars were synthesized by coating an epoxy-based SU-8 photoresist (SU-8, MicroChem) on a thin cover slip (170 μm thick). The SU-8 film was cured into a structured array pattern of micropillars (pillar diameter: $d = 30$ μm; center-to-center distance: $l = 60$ μm; height: $h = 20$ μm), utilizing photolithography. After UV-exposure (8 s) using a photomask and baking cycles at 65 °C (30 min), 95 °C (3 min), and 65 °C (30 min), the uncured SU-8 was dissolved in a developer solution and washed in propanol. For gas-layer infused micropillars, the array was infiltrated with the stoichiometric ratios of (see below) gas-forming layer (NaHCO$_3$–C$_6$H$_8$O$_7$ at 20 mg mL^{-1} in acetone) by spray-coating (0.3 mL s^{-1} at 2 bars, 0.5 mm nozzle diameter). After polishing, the loading is sufficiently low such that the tops of the pillars are still clearly visible. 10 mL were deposited per area of 6 cm × 2.5 cm. The

**ADVANCED
SCIENCE NEWS**

www.advancedsciencenews.com

**ADVANCED
FUNCTIONAL
MATERIALS**

www.afm-journal.de

Figure 5. Drop impact on soot-templated, EC–SH (bilayered), and Quad-layered surfaces. a) The drop (6 μm diameter) impacts the surface at a preset velocity depending on deposition height (up to ≈1 m). A set of velocities (from 1 to 6 m s^{-1}) was used and contact time assessed. b) Beyond 3 m s^{-1}, soot-templated surfaces appear to be penetrated, leaving tiny drop remnants while maintaining a steady increase in contact time. The data points showing impalement is indicated with a cross (+), with minor impalement colored yellow and severe impalement colored red. Drop contact time was analyzed via an algorithm, measuring the time taken for a drop to lose contact with the surface. c–e) Over the range of test velocities, the drops that impacted the EC–SH and Quad-layered surfaces appear to experience fragmentation, as compared to minimal fragmentation for those impacting soot-templated surfaces. EC: ethyl cellulose polymer; GL: gas-forming layer; PVP: polyvinylpyrrolidone; SH: superhydrophobic/superamphiphobic. Quad layer: EC–GL–PVP–SH.

final functional layer (see synthesis below) of hydrocarbon- or fluoro-functionalized silica (suspended at 10 mg mL^{-1} acetone) was spray-coated (0.2 mL s^{-1} at 2 bars, 0.3 mm nozzle diameter) at 10 mL over an area of 6 cm × 10 cm. CO$_2$ formers were chosen after assessing H2 and N2 formers, which suffered from a) poor long-term gas stability (H$_2$, Movie S8, Supporting Information) after powdered processing, and b) poor dispersibility (N$_2$, Movie S9, Supporting Information).

Testing Model Surfaces (Confocal Microscopy): An inverted laser scanning confocal microscope (Leica TCS SP8) was used to monitor the top-down progression of the contact line during the wetting of water of model micropillar arrays. Lasers of 458 and 488 nm were used at ≈15% power. Water was dyed with ATTO 488 at 10 μg mL^{-1}. A dry objective, Leica HC PL APO 10×, NA 0.4 was used at 2.25× digital zoom, at an fps of 0.44–2 s^{-1}. A water drop of 2 μL was added to the test surfaces using a syringe needle (30G) fixed at ≈1 mm above the surface. Water was pumped in at 0.02 μL s^{-1}.

Testing of Plastron Stability: Pressure Testing with Model Surfaces: A custom-built pressure chamber (10 mL) with an imaging window (1 mm thick glass at 1 cm diameter) was used with a pressure transducer (RSPRO 175–5042, 0–150 psig) and syringe pump (Sonotek T1). A 5 mL Terumo syringe was used with at a flow rate of 1 mL min^{-1} to pressurize the chamber. A USB microscope (Toolcraft, Microcapture Plus) was mounted onto the chamber to observe changes in plastron behaviors at ≈36× magnification. Plastron reflectivity was then analyzed through a custom MATLAB algorithm that computes the brightness of the plastron from the RGB image. Multiple zones were analyzed and averaged for representation. To avoid the microlensing effect from plastrons that

are collapsing between bare pillars, the binary thresholding algorithm (imbinarize) was also used.

Long Term Immersion (Gas Analysis) of Multilayered (or Part Thereof) Surfaces: An imaging setup for plastron robustness during immersion utilized glass tubes of 40 mL in volume (2.5 cm diameter). Tubes were filled with milliQ deionized water, before immersing glass slides with superhydrophobic/superamphiphobic coatings. On various coatings, the air plastron was then replaced by injecting H$_2$, N$_2$, and CO$_2$ gases in excess, bubbling 1 mL per surface (1.25 cm × 6 cm). Any excess gases were bubbled away into the atmosphere. Tubes were then sealed and plastrons were observed and imaged over time. Immersion depth ranges from 1 to 5 cm depending on the depth of the coating.

Long Term Immersion (Wetting Analysis) of Multilayered Surfaces: Control and test surfaces were also immersed into a bath (8 L) of milliQ deionized water at a height of 20 cm for 8 weeks. The temperature in the laboratory varied between 15 and 20 °C during this period. Wettability tests and scanning electron microscopy were performed before and after immersion.

Synthesis of Multilayered Surfaces: Control soot-templated surfaces were fabricated per the multistep protocol highlighted in *Science* **2012**, 335, 67.[43] This method creates a soot-templated silica shell (primary layer), before a secondary layer of fluoro-functionalization. The multilayered hierarchical "Quad" surfaces were synthesized as follows: 1) EC was dissolved (0.05 g mL^{-1}) in a binary solvent (toluene:acetone at 4:1 v/v ratio). This layer was spin-coated onto glass slides (170 μm or 1 mm) depending on use at 500 RPM, 60 s. 2) The GL was synthesized from a stoichiometric ratio (1:3) of NaHCO$_3$–C$_6$H$_8$O$_7$, typically 1 g: 0.76 g.

Other GL configurations were tested, including CO_2 forming ($NaHCO_3$–$C_6H_8O_6$; Ascorbic acid), H_2 forming (Powdered calcium metal), and N_2 forming ($NaNO_2$–H_2NSO_3). This layer was dispersed at 20 mg mL^{-1} in acetone and spray-coated (0.3 mL s^{-1} at 2 bars, 0.5 mm nozzle diameter) onto the first layer at 10 mL per area of 7.5 cm × 2.5 cm. This layer is moisture sensitive and should be deposited under an inert environment (N_2) to prevent acetone-evaporation induced condensation whenever possible. A wait time of 30 min was allowed before deposition of the third layer. 3) The condensation-protection layer (polyvinylpyrrolidone M_w 53k, PVP), was deposited (20 mg mL^{-1} ethanol) using spin-coating at 2000 RPM, 60 s. 0.5 mL s^{-1} of the solution was placed at the center of the glass slide during spinning at 2000 RPM. EC is soluble in ethanol and this creates an encapsulation layer without coating dissolution. 4) The final functional layer of hydrocarbon- or fluoro-functionalized silica (suspended at 10 mg mL^{-1} acetone) was spray-coated (0.2 mL s^{-1} at 2 bars, 0.3 mm nozzle diameter) at 40 mL over an area of 7.5 cm × 10 cm. The synthesis of both the hydrocarbon- or fluorocarbon-functionalized silica (in chloroform) follows the recipe (in stoichiometric excess) presented by Wong.[36] The hydrocarbon-functionalized silica is only superhydrophobic while the fluorocarbon-functionalized silica is superamphiphobic (liquids of surface tension at ≈27 mN m^{-1} slides off). All chemicals were purchased from Sigma-Aldrich.

Wetting Testing: Contact Angles: Dynamic and static contact angles were recorded using an OCA 35 contact angle goniometer (Dataphysics, Germany, zoom factor 1.0). Roll-off angles were assessed by tilting the surfaces at 1° s^{-1} until the drop (6 µL) starts rolling off (20 ms per frame). The contact angles and roll-off angles were computed by a commercially available program (SCA20). Results are presented as mean ± standard deviations. Liquids tested include water, ethylene glycol, sunflower oil, hexadecane, n-decane, and ethanol:water at 20%, 40%, and 60%.

Scanning Electron Microscopy: Surfaces with different layers were coated with a thin layer of platinum (7 nm) using sputtering, before analysis with scanning electron microscopy (Zeiss, LEO 1530 Gemini). A working voltage of 3 kV, coupled to an aperture of 10 µm, and a working distance of 2 mm was used.

Drop Impact Testing: The drop impact of single drops was analyzed optically using a high-speed camera (20 000 fps, Photron Fastcam Mini AX10, Japan). An objective at 1× (Edmund Optics) was used. Deionized water drops (8 µL) were released from various heights (5 to 100 cm). The approach velocity was tuned by the distance of release. This ranged from 1 to 6 m s^{-1}. Imaging was performed at 10 000 fps from 5 to 60 cm. As the drop begins to change its path beyond a drop height of 60 cm, the imaging domain was increased, at the expense of a lower frame rate of 6000 fps from 60 to 100 cm.

Supporting Information

Supporting Information is available from the Wiley Online Library or from the author.

Acknowledgements

Conflict of Interest

The authors declare no conflict of interest.

Author Contributions

W.S.Y.W. designed the experiments, fabricated the surfaces, and carried out the experiments and characterization unless otherwise stated below and wrote the manuscript. W.S.Y.W. and D.V. contributed to experimental planning, data analysis, and manuscript preparation. All authors reviewed and approved the manuscript.

Data Availability Statement

The data that supports the findings of this study are available in the main article and the supplementary material of this article.

Keywords

[1] Y. A. Mehanna, E. Sadler, R. L. Upton, A. G. Kempchinsky, Y. Lu, C. R. Crick, *Chem. Soc. Rev.* **2021**, *50*, 6569.

[2] F. Geyer, M. D'Acunzi, C.-Y. Yang, M. Müller, P. Baumli, A. Kaltbeitzel, V. Mailänder, N. Encinas, D. Vollmer, H.-J. Butt, *Adv. Mater.* **2019**, *31*, 1801324.

[3] L. Li, Y. Bai, L. Li, S. Wang, T. Zhang, *Adv. Mater.* **2017**, *29*, 1702517.

[4] X. Su, H. Li, X. Lai, Z. Chen, X. Zeng, *ACS Appl. Mater. Interfaces* **2018**, *10*, 10587.

[5] J. Wang, Y. Zheng, F.-Q. Nie, J. Zhai, L. Jiang, *Langmuir* **2009**, *25*, 14129.

[6] L. Rapoport, T. Emmerich, K. K. Varanasi, *Adv. Mater. Interfaces* **2020**, *7*, 1901599.

[7] K. I. Hegner, W. S. Y. Wong, D. Vollmer, *Adv. Mater.* **2021**, *33*, 2101855.

[8] W. S. Y. Wong, A. Naga, L. Hauer, P. Baumli, H. Bauer, K. I. Hegner, M. D'Acunzi, A. Kaltbeitzel, H.-J. Butt, D. Vollmer, *Nat. Commun.* **2021**, *12*, 5358.

[9] L. R. J. Scarratt, U. Steiner, C. Neto, *Adv. Colloid Interface Sci.* **2017**, *246*, 133.

[10] C. Shi, X. Cui, X. Zhang, P. Tchoukov, Q. Liu, N. Encinas, M. Paven, F. Geyer, D. Vollmer, Z. Xu, H.-J. Butt, H. Zeng, *Langmuir* **2015**, *31*, 7317.

[11] G. Liu, W. S. Y. Wong, M. Kraft, J. W. Ager, D. Vollmer, R. Xu, *Chem. Soc. Rev.* **2021**, *50*, 10674.

[12] H. E. Hinton, *Nature* **1966**, *209*, 220.

[13] W. Barthlott, T. Schimmel, S. Wiersch, K. Koch, M. Brede, M. Barczewski, S. Walheim, A. Weis, A. Kaltenmaier, A. Leder, H. F. Bohn, *Adv. Mater.* **2010**, *22*, 2325.

[14] A. Tuteja, W. Choi, G. H. McKinley, R. E. Cohen, M. F. Rubner, *MRS Bull.* **2008**, *33*, 752.

[15] M. Callies, D. Quéré, *Soft Matter* **2005**, *1*, 55.

[16] A. Cassie, S. Baxter, *J. Chem. Soc., Faraday Trans.* **1944**, *40*, 546.

[17] R. N. Wenzel, *Ind. Eng. Chem. Res.* **1936**, *28*, 988.

[18] P. Lv, Y. Xue, Y. Shi, H. Lin, H. Duan, *Phys. Rev. Lett.* **2014**, *112*, 196101.

[19] R. Poetes, K. Holtzmann, K. Franze, U. Steiner, *Phys. Rev. Lett.* **2010**, *105*, 166104.

[20] J. Seo, R. García-Mayoral, A. Mani, *J. Fluid Mech.* **2018**, *835*, 45.

[21] M. Xu, G. Sun, C.-J. Kim, *Phys. Rev. Lett.* **2014**, *113*, 136103.

[22] D. Panchanathan, A. Rajappan, K. K. Varanasi, G. H. McKinley, *ACS Appl. Mater. Interfaces* **2018**, *10*, 33684.

[23] M. Xu, C. T. Liu, C.-J. Kim, *Langmuir* **2020**, *36*, 8193.

[24] B. P. Lloyd, P. N. Bartlett, R. J. K. Wood, *ACS Omega* **2021**, *6*, 3483.

[25] T. N. Krupenkin, J. A. Taylor, E. N. Wang, P. Kolodner, M. Hodes, T. R. Salamon, *Langmuir* **2007**, *23*, 9128.

[26] C. Lee, C.-J. Kim, *Phys. Rev. Lett.* **2011**, *106*, 014502.

[27] S. Adera, R. Raj, R. Enright, E. N. Wang, *Nat. Commun.* **2013**, *4*, 2518.

[28] Z. Li, J. Marlena, D. Pranantyo, B. L. Nguyen, C. H. Yap, *J. Mater. Chem. A* **2019**, *7*, 16387.

[29] M. N. Kavalenka, F. Vüllers, S. Lischker, C. Zeiger, A. Hopf, M. Röhrig, B. E. Rapp, M. Worgull, H. Hölscher, *ACS Appl. Mater. Interfaces* **2015**, *7*, 10651.

[30] T. Verho, J. T. Korhonen, L. Sainiemi, V. Jokinen, C. Bower, K. Franze, S. Franssila, P. Andrew, O. Ikkala, R. H. A. Ras, *Proc. Natl. Acad. Sci. USA* **2012**, *109*, 10210.

[31] C. F. Carlborg, W. van der Wijngaart, *Langmuir* **2011**, *27*, 487.

[32] R. Hensel, R. Helbig, S. Aland, H.-G. Braun, A. Voigt, C. Neinhuis, C. Werner, *Langmuir* **2013**, *29*, 1100.

[33] T. L. Liu, C.-J. C. Kim, *Science* **2014**, *346*, 1096.

[34] X. Jiao, M. Li, X. Yu, W. S. Y. Wong, Y. Zhang, *Chem. Eng. J.* **2021**, *420*, 127606.

[35] H.-J. Butt, C. Semprebon, P. Papadopoulos, D. Vollmer, M. Brinkmann, M. Ciccotti, *Soft Matter* **2013**, *9*, 418.

[36] W. S. Y. Wong, *Nano Lett.* **2019**, *19*, 1892.

[37] W. S. Y. Wong, K. I. Hegner, V. Donadei, L. Hauer, A. Naga, D. Vollmer, *Nano Lett.* **2020**, *20*, 8508.

[38] P. Papadopoulos, D. Vollmer, H.-J. Butt, *Phys. Rev. Lett.* **2016**, *117*, 046102.

[39] W. S. Y. Wong, T. P. Corrales, A. Naga, P. Baumli, A. Kaltbeitzel, M. Kappl, P. Papadopoulos, D. Vollmer, H.-J. Butt, *ACS Nano* **2020**, *14*, 3836.

[40] L. Hauer, W. S. Y. Wong, V. Donadei, K. I. Hegner, L. Kondic, D. Vollmer, *ACS Nano* **2021**, *15*, 4658.

[41] B. Vogt, C. Soles, H.-J. Lee, E. Lin, W. Wu, *Polymer* **2005**, *46*, 1635.

[42] S. A. McBride, H.-L. Girard, K. K. Varanasi, *Sci. Adv.* **2021**, *7*, 6960.

[43] X. Deng, L. Mammen, H.-J. Butt, D. Vollmer, *Science* **2012**, *335*, 67.

[44] T. Deng, K. K. Varanasi, M. Hsu, N. Bhate, C. Keimel, J. Stein, M. Blohm, *Appl. Phys. Lett.* **2009**, *94*, 133109.

[45] T. Vasileiou, J. Gerber, J. Prautzsch, T. M. Schutzius, D. Poulikakos, *Proc. Natl. Acad. Sci. USA* **2016**, *113*, 13307.

[46] G. B. Foote, P. S. Du Toit, *J. Appl. Meteorol. Climatol.* **1969**, *8*, 249.

[47] J. C. Maxwell, *Nature* **1874**, *10*, 119.

[48] J. C. Bird, R. Dhiman, H.-M. Kwon, K. K. Varanasi, *Nature* **2013**, *503*, 385.

[49] A. Tuteja, W. Choi, M. Ma, J. M. Mabry, S. A. Mazzella, G. C. Rutledge, G. H. McKinley, R. E. Cohen, *Science* **2007**, *318*, 1618.